COMMUNICATION

Improved High-Current-Density Hydrogen Evolution Reaction Kinetics on Single-Atom Co Embedded in Order Pore Structured Nitrogen Assembly Carbon Support

Received 00th January 20xx,
Accepted 00th January 20xx

DOI: 10.1039/x0xx00000x

Jiaqi Yu[a]†, Yu Yan[b]†, Yuemin Lin[a,f]†, Hengzhou Liu[c], Yuting Li[d], Shaohua Xie[e], Simin Sun[a], Fudong Liu[e], Zhiguo Zhang[f], Wenzhen Li[c], Jin-Su Oh[d], Lin Zhou[d], Long Qi[d]*, Bin Wang[b]*, Wenyu Huang[a,d]*

Single-atom catalysis is a subcategory of heterogeneous catalysis with well-defined active sites. Numerous endeavors have been devoted to developing single-atom catalysts for industrially applicable catalysis, including hydrogen evolution reaction (HER). High current density electrolyzers have been pursued for single-atom catalysts to increase active site density and enhance mass transfer. Here, we reason that single-atom metal embedded in nitrogen assembly carbon (NAC) catalysts with high single-atom density, large surface area, and ordered mesoporosity, could fulfill the industrially applicable HER. Among several different single-atom catalysts, the HER overpotential with the best performing Co-NAC reaches 200 mA cm^{-2} current density at 310 mV, relevant to industrial applicable current density. Density functional theory (DFT) calculations suggest the feasible hydrogen binding on single-atom Co results in the promising HER activity over Co-NAC. The best-performing Co-NAC shows robust performance under alkaline conditions at 50 mA cm^{-2} current density for 20 h in an H-cell and at 150 mA cm^{-2} current density for 100 h in a flow cell.

Introduction

To achieve net-zero carbon emissions, clean and renewable energy resources draw extensive attention for sustainable development and deployment. Green hydrogen generated from water electrocatalytic splitting is recognized as one of the most promising clean fuels when the electricity comes from renewable sources such as wind, solar, and hydropower. To accommodate both hydrogen and oxygen evolution reactions in the same electrolyte solutions, hydrogen evolution reaction (HER) under alkaline conditions is more desirable to simplify the water splitting process due to the sluggish kinetics of oxygen evolution reaction (OER) under acidic conditions.[1] Under alkaline conditions, Pt-based catalysts are superior for HER although the high cost with limited supply restricts their large-scale applications.[2-6] Alternatively, earth-abundant metal catalysts have gained significant attention for HER such as Ni, Co, and Mo_2C.[7-11]

Numerous efforts have been devoted to developing single-atom catalysts because of their high atomic utilization and unique activity in contrast to nanomaterials.[12, 13] The kinetics of single-atom catalysts are critically dependent on the loading of the active sites, the interaction between metal and support, and the support structure. In particular, the porous supports with high surface area usually lead to reduced mass transfer limitation and, hence, improved catalytic kinetics.[14] In electrocatalytic reactions, the conductivity of the catalyst is another essential factor affecting activities. Some single-atom catalysts with 3*d* transition metals, such as Fe-N-C, Co-TiO_2, and Co-N-C, showed promising activity for HER with low onset potentials that are comparable to precious metal catalysts.[15-19] Nevertheless, atomically-dispersed non-precious metal HER catalysts remain to be further developed and investigated to suit industrial applications, especially under large currents.

Herein, we designed single-atom catalysts with nitrogen assembly carbon (NAC) as an ordered porous support to study HER at high current density under alkaline electrolyte conditions.[20] The high nitrogen content of NAC support enables the regulated anchoring of five 3*d* to 5*d* metals (e.g., Co, Fe, Ni, Cu, and Ru) generally with high metal site loading. The high surface area combined with the ordered mesoporous structure ensures high surface exposure of metal sites and facilitates mass transfer under large currents and fast reaction kinetics for alkaline HER. Among all studied catalysts, Co-NACs exhibit the

[a] Department of Chemistry, Iowa State University, Ames, IA 50011 USA. E-mail: whuang@iastate.edu
[b] School of Chemical, Biological and Materials Engineering, University of Oklahoma, Norman, OK, 73019 USA. E-mail: wang_cbme@ou.edu
[c] Department of Chemical and Biological Engineering, Iowa State University, Ames, IA 50011, USA
[d] U.S. DOE Ames National Laboratory, Iowa State University, Ames, IA 50011, USA. E-mail: lqi@iastate.edu
[e] Department of Chemical and Environmental Engineering, University of California, Riverside, CA 92521, United States
[f] Key Laboratory of Biomass Chemical Engineering of Ministry of Education, College of Chemical and Biological Engineering, Zhejiang University, Hangzhou 310058, P.R. China
† These authors contributed equally to this work.
Electronic Supplementary Information (ESI) available: [details of any supplementary information available should be included here]. See DOI: 10.1039/x0xx00000x

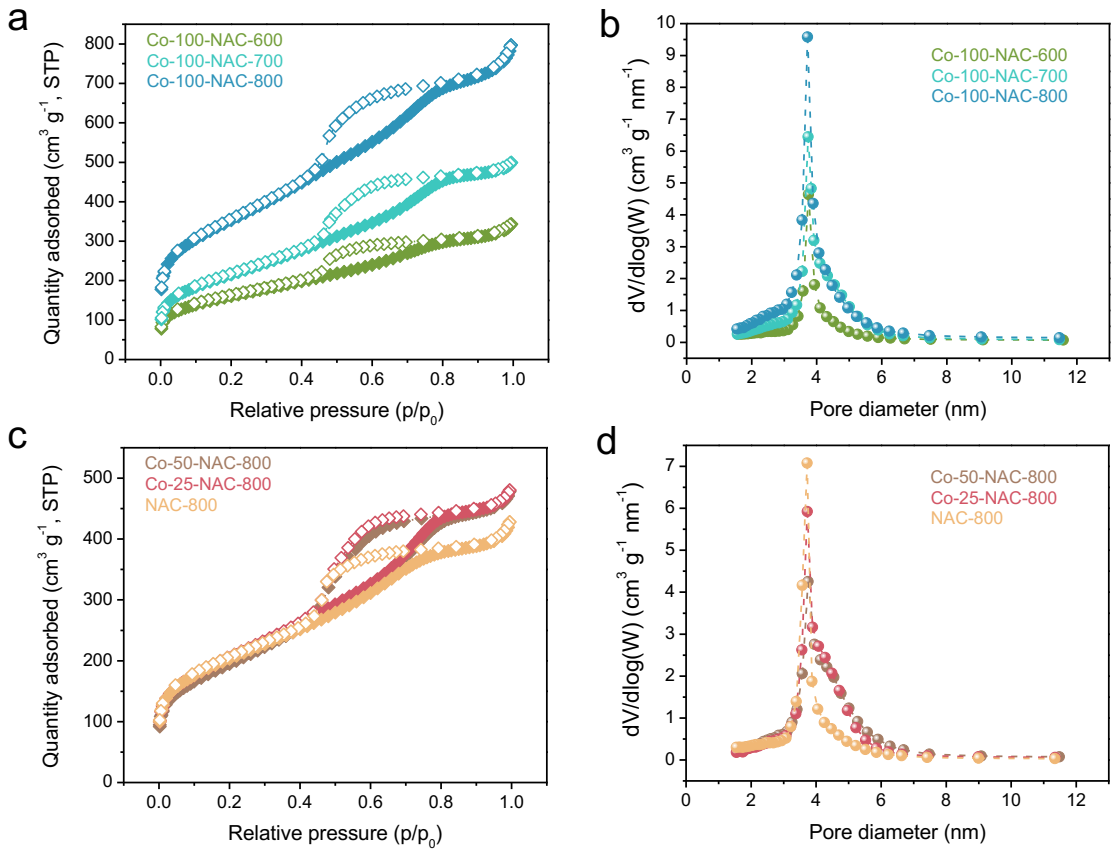

Figure 1. N_2-sorption isotherm (a,c) and pore size distribution (b,d) of Co-NAC catalysts carbonized at 600, 700, and 800 ºC with different metal loadings. The samples are named as Co-x-NAC-y, which are prepared with x mg of added $Co(acac)_2$ and under y ºC carbonization temperature. The actual Co loadings are summarized in Table S1. NAC-800 is a sample prepared using the same method but without adding Co precursor.

best performance with the smallest overpotential followed by a rapid current increase. The synthesis of Co-NAC was further optimized by varying the Co loading and the carbonization temperature. Co-100-NAC-800, prepared at 800 °C with the highest Co single atom loading (1.9 wt.%), reaches 200 mA cm^{-2} at 310 mV overpotential, during the linear sweep voltammetry (LSV) test. The Tafel slope of Co-NAC materials is over 130 mV dec^{-1}, indicating that the Volmer step is rate-determining. The density functional theory (DFT)-calculated free energy diagram suggests such outstanding HER activity is due to moderate binding of hydrogen over Co-NAC with various nitrogen coordination. The high robustness of Co-100-NAC-800 was further demonstrated by stable potential over a 100-hour test at 125 mA cm^{-2} current density in a membrane electrode assembly (MEA).

Results & discussions

Synthesis and Characterization of single-atom NAC

Single-atom metal-NAC catalysts were prepared following a reported hard-template method (shown in **Scheme S1**).[21, 22] Ethylenediamine firstly coordinated with metal precursors as the acetylacetonate salt (for Co, Ni, Fe, Cu, and Ru) and polymerized with tetrachloride carbon, using SBA-15 silica with a long-range ordered mesopore structure as the template. The resulting mixture was carbonized under Ar at different temperatures ranging from 600 to 800 °C. The single-atom NAC was obtained after removing SBA-15 template upon etching. We designate the as-prepared single-atom NAC samples as M-x-NAC-y, where M represents the metal type, x denotes the mass of metal precursor added in milligrams, and y indicates the carbonization temperature in degrees Celsius. For instance, Co-100-NAC-800 stands for a cobalt single-atom catalyst embedded in NAC, prepared using 100 mg of cobalt precursor and carbonized at 800 °C.

Using Co-NAC as an example, the powder X-ray diffraction (PXRD) patterns in **Figure S1** show primarily two peaks at 25° and 44° assigned to graphitic carbon structure, while no peak was observed for metallic Co particles. The N_2 physisorption studies show that the surface areas of the prepared Co-NACs are typically larger than 600 $m^2 g^{-1}$ (**Figure 1** and **Table S2**). The mesoporous structures were indicated by the Type IV hysteresis loop observed from N_2 adsorption/desorption isotherm curves (**Figure 1a** and **1c**). Pore distribution simulated with the BJH model confirmed the ordered mesoporous structure of Co-NAC with an average pore size at around 4.0 nm (**Figure 1b** and **1d** and **Table S2**). The large surface area and the ordered mesoporous morphology hold the promise of improved mass transfer, which could facilitate the high current density electrochemical applications at the industrial scale.

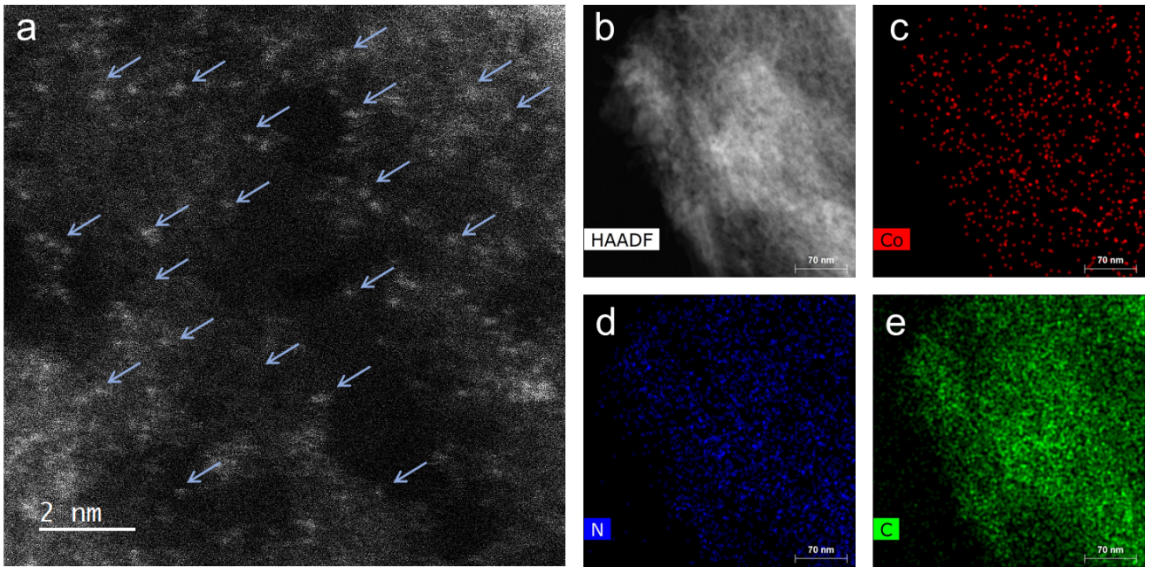

Figure 2. Electron microscopy characterization of Co-100-NAC-800. (a) HR-STEM image of Co-NAC, the arrows indicate the single atom Co on the NAC support. (b-e) EDS elemental mapping images of Co-NAC: (b) HAADF-STEM image; (c) Co mapping; (d) C mapping; (e) N mapping.

Additionally, the scanning electron microscope (SEM) and transmission electron microscope (TEM) images show the synthesized Co-NAC preserved the morphology and aligned pore structure of the SBA-15 template (**Figures S2 and S3**).

High-resolution scanning transmission electron microscope (HR-STEM) study of the representative Co-100-NAC-800 reveals single Co atoms embedded on NAC, with no observable nanoparticles or clusters (**Figure 2a**; Co single atoms are indicated by blue arrows). The uniform distribution of Co on the NAC substrate was confirmed through energy dispersive X-ray spectroscopy (EDS) elemental mapping (**Figures 2b-e**), Indicating the successful preparation of the single-atom Co-NAC catalysis.

X-ray absorption experiments of the Co K-edge were carried out for representative Co-NAC samples. As shown in **Figure S5a**, X-ray absorption near edge structure (XANES) spectra of all three samples present a higher energy pre-edge and a more intense white line than Co foil, suggesting oxidized Co species. The XANES spectra of Co-NAC catalysts are consistent with 4-coordinate cobalt atoms reported in literature.[23-25] In the extended X-ray absorption fine structure (EXAFS) spectra, only one main peak is observed for the first shell (**Figure S5b**). Fittings of the EXAFS spectra with defined coordination numbers of 4 for all samples gave bond lengths of 1.94, 1.94 and 1.99 Å (**Figure S6** and **Table S3**) for Co-NAC-800, -700, and -600, respectively, best assigned as Co-N bonds.[26, 27] There is no detection of Co-Co at 2.49 Å (after phase correction) in the second shell. Consequently, the results of XANES and EXAFS analysis suggest cobalt atoms are atomically dispersed and bonded with most likely four nitrogen atoms on the NAC support. X-ray photoelectron spectroscopy (XPS) suggests that the Co species in the Co-NAC are majorly Co^{2+}, while there are several N species, including graphitic, pyrrolic, and pyridinic N, existing in the Co-NAC (as shown in **Figure S7**).

Electrocatalytic hydrogen evolution reaction

Screening of the HER activity over different metal-NACs was carried out under alkaline electrolyte (1M KOH) in a H-cell. Carbon fiber paper (1 cm^2) with single-atom catalyst deposit, Hg/HgO (1M KOH), and Pt mesh were used as the working, reference, and counter electrodes, respectively. Nafion 117 membrane was used to separate the cathode and anode. LSV was performed from 0 to –0.5 V versus reverse hydrogen electrode (RHE) to monitor the HER performance of metal-NACs and compared with metal-free NAC-800 support and commercial Pt/Vulcan. Fe-100-NAC-800, Co-100-NAC-800, and Ni-100-NAC-800 show similar current change behavior with larger overpotential than Pt/Vulcan but rapid current increase, while Cu-NAC and Ru-NAC show sluggish HER over the test range (**Figure S8**). Among these catalysts, Co-100-NAC-800 demonstrates the smallest overpotential, 207 mV at 10 mA cm^{-2} and 292 mV at 50 mA cm^{-2}. The rapid current increase for Co-NAC permits high current density HER under relatively small overpotential compared to the single-atom catalysts reported in literature.[12, 14, 17]

We further performed HER in a single cell with Co-NAC catalysts to test the effect of varied synthetic parameters. The single cell setup helps eliminate the cation exchange limitation on the Nafion membrane at high current density. Synthetic parameters, particularly carbonization temperature, can directly impact catalysts physiochemical properties including the N content of NAC support (**Table S4**), local coordination of metal sites, conductivity, and surface area. Besides, the density of catalytically active sites is essential for the high-current HER application. Therefore, Co-NAC catalysts were prepared and examined for the large current HER with different amounts of Co precursors and carbonized at different temperatures. The exact Co loading was measured using inductively coupled

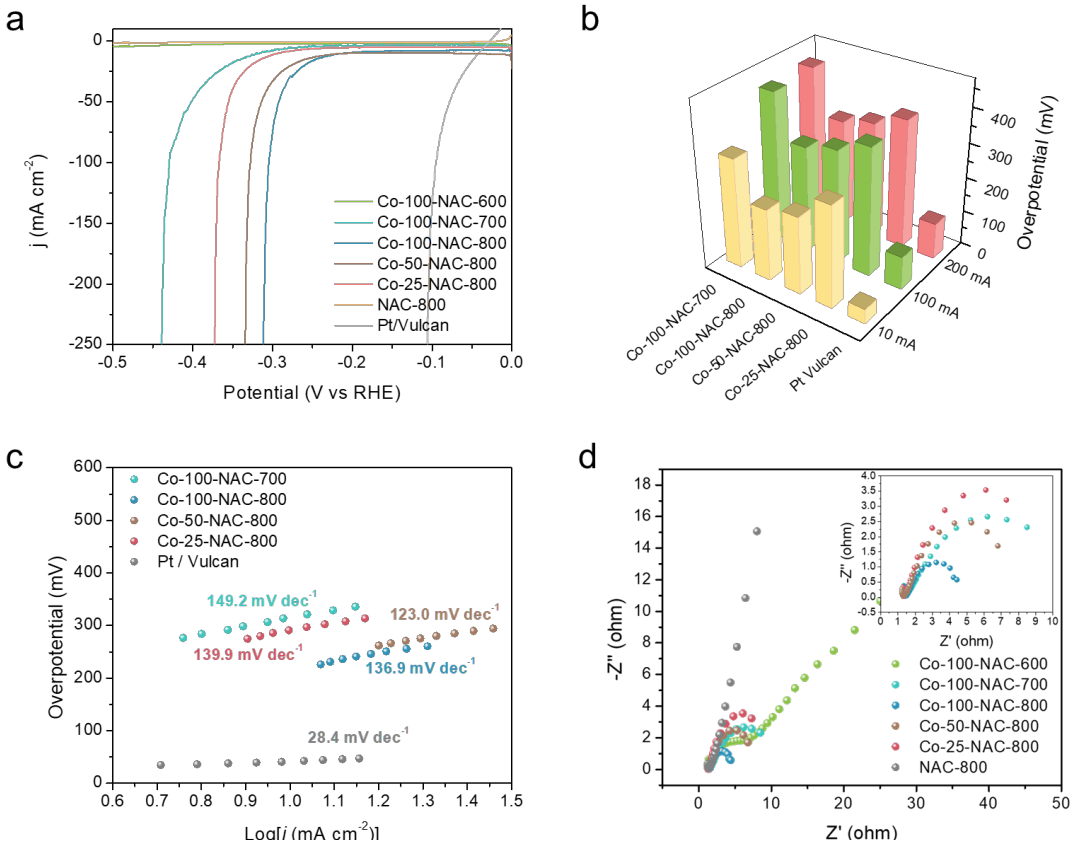

Figure 3. HER evaluation on Co-NAC. (a) LSV; (b) Overpotential at 10, 100, and 200 mA cm^{-2}; (c) Tafel plots; (d) Nyquist plots at −0.3 V; insert: zoom-in Nyquist plot. Co-100-NAC-600 overlaps with NAC-800 in (a).

plasma mass spectrometry (ICP-MS), **Table S1**. From the LSV profile of Co-NACs shown in **Figure 3a**, Co-100-NAC-800 prepared at 800 °C with the highest Co loading shows the smallest overpotential, 310 mV at 200 mA cm^{-2} current density. Co-NAC catalysts prepared at lower temperatures have a larger onset overpotential; in contrast, Co-100-NAC-600 shows negligible activity in HER within the tested potential range. Like Co-100-NAC-800, Co-100-NAC-700 also enables a rapid current increase but starts at a larger overpotential after a considerable window of the sluggish current response. As summarized in **Figure 3b**, the trend of HER overpotential change with respect to Co loadings of Co-NAC-800 catalysts aligns with our prediction that catalysts with high Co loading provide more active sites for HER, improve the overall kinetics, and lower the HER overpotential at high current density.

The Tafel plots of Co-NAC catalysts provide insight into the HER mechanism, shown in **Figure 3c**.[28] In the low current density region, Co-NAC catalysts present a Tafel plot larger than 120 mV dec^{-1}, indicating the Volmer step as the rate-determining step.[28] It is generally accepted that the good conductivity of electrodes is more desirable in the electrocatalytic process to maximize electron utilization efficiency.[29] Electrochemical impedance spectroscopy (EIS) was conducted to study the conductivity properties of Co-NACs under 300 mV overpotential. As shown from the Nyquist plot in **Figure 3d**, the resistances of the Co-100-NAC-800 are better than Co-100-NAC-600 and -700. With better conductivity, the joule loss of Co-100-NAC-800 at high current density is smaller than those of Co-100-NAC-600 and -700.

Electrode surface area can affect mass transfer, especially under large current conditions. Large electrode surface areas are therefore pursued to eliminate the mass transfer limitation. The electrochemical surface areas (ECSA) of Co-NACs were estimated using double-layer capacitance (C_{dl}), as shown in **Figures S9-S14**. Cyclic voltammetry (CV) was performed at different scanning rates in a potential range without any faradaic process. The slope of current density versus scanning rate is the double-layer capacitance of the Co-NAC electrode, and the ECSA can be calculated using the ratio between C_{dl} and specific capacitance (C_s), shown in **Equation 1**. Measuring the materials' C_s involves an unachievable flat electrode with this single-atom porous material. However, researchers have measured a series of materials for their specific capacitance, which typically ranges between 0.022 to 0.130 mF cm^{-2} in alkaline electrolytes.[30, 31] In this case, we estimate the ECSA of Co-NAC using C_s = 0.06 mF cm^{-2}. As mentioned above, the NAC support has a large surface area and ordered mesoporous structure; as a result, the corresponding ECSA of NAC catalysts is calculated to be from 531.7 to 2455 cm^2 (per cm^2 geometric electrode surface). The large ECSA maximizes active site exposure and thus minimizes the mass transferring limitation, which makes HER at high current density feasible.

$$ECSA = \frac{C_{dl}}{C_s} \quad (1)$$

The durability of electrodes is a crucial parameter for industrial applications. Enhancing durability under high current density is challenging because the large current could change the structure of the electrode leading to site deactivation or metal leaching. A 20 h stability test was performed at 50 mA cm^{-2} current density in 1M KOH electrolyte with stirring. As shown in **Figure 4a**, the potential remained unchanged over the 20 h test with the Co-100-NAC-800 catalyst. At the same time, the hydrogen bubble was continuously generated from the electrode (shown in **Figure S15** and supplementary video). No structure evolution of Co-100-NAC-800 was observed from the XRD pattern after the 20-h stability test (**Figure S16**).

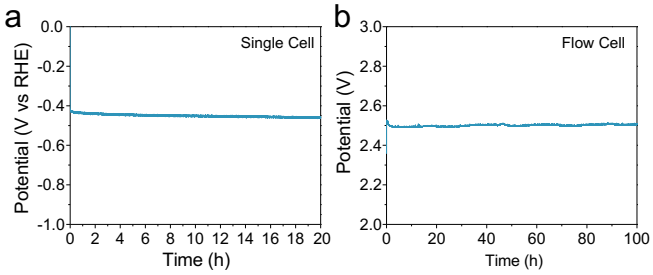

Figure 4. Stability test of Co-100-NAC-800. (a) chronopotentiometry (CP) plot showing the stability test at 50 mA cm^{-2}; (b) 100 h water splitting test in flow cell with Co-100-NAC-800 as cathode catalyst and Pt on carbon as anode catalyst.

To evaluate the long-term stability of the Co-NAC under practical conditions, we conducted a continuous flow test. A membrane electrode assembly (MEA) was built with Co-100-NAC-800 as the cathode catalyst and Pt/Vulcan as anode catalyst to test the stability of Co-NAC catalyst. As shown in **Figure 4b**, the initial voltage of the water splitting is 2.50 V at a current density of 150 mA cm^{-2}. Despite the observed overpotential of water splitting being compromised by the sluggish OER on the Pt electrode, the cell voltage kept stable at 2.50 V during the 100 h stability test with no voltage increase.

Theoretical insight

DFT calculations were performed to provide insights of the potential atomic structure of the potential active sites for HER. Gibbs free energy of H adsorption was used as a descriptor for the HER activity as in literature.[32, 33] **Figure 5** shows that the H binding energy on the CoN_4 is 0.18 eV. As indicated in our previous study, the binding configuration between the single metal atom and the substrate atom (nitrogen or carbon) could be altered among the coordination (N_xC_{4-x}) of the NAC.[22] Thus, DFT calculations were carried out on Co-NAC with these possible coordinations shown in **Figure 5**. To compare their metal-substrate binding configuration, the values with varied bond lengths between the Co and N (or C) atoms are provided in **Table S5**. The shorter metal-support bond and the increased number of N coordination enable the CoN_4 structure to have stronger metal-substrate interaction in agreement with the EXAFS results (**Figures S2** and **S3**). The HER energy profiles of Co-NACs were further investigated for different Co-N_x-NAC structures. The varied N coordination moderates the Co-H binding, with the CoN_3C_1 showing the least free energy difference for H adsorption on the metal centre, indicating the lowest overpotential based on the computational hydrogen electrode (CHE) model.[34] The thermodynamic calculations in

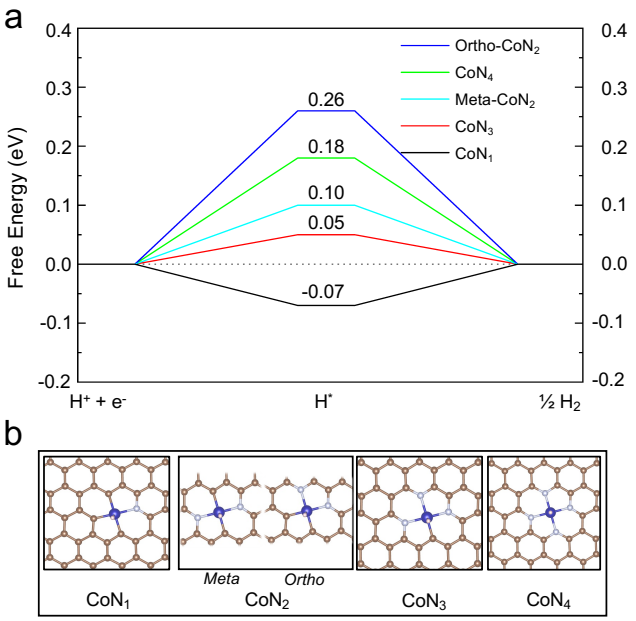

Figure 5. DFT calculations of hydrogen adsorption. (a) Calculated HER free energy diagram over different configurations of Co-N_x-NAC. The H binding energy is labeled on the top of each configuration. (b) Atomic structures of H adsorbed on Co-N_x-NAC.

Figure 5 thus suggest that Co-NACs, possibly with the CoN_3 site, could also show promising HER activity. Our DFT calculations cannot unambiguously determine the exact local binding configuration of Co (e.g., N_4 vs N_3C_1) in Co-NAC, and in the real samples, different metal-coordination likely coexist; nevertheless, the calculations reveal that single-atom Co with various Co-N coordination displays favorable hydrogen binding that is close to thermoneutral at the metal centre.

Conclusions

We systematically studied the single atom Co materials, Co-NACs, which efficiently catalyze the hydrogen evolution reaction (HER) under high current density. The synthetic parameters, including Co metal loading and carbonization temperature, were varied as critical parameters for the HER performance studies. High Co loading and high carbonization temperature lead to low overpotential and high current density. On the contrary, low carbonization temperature results in large resistance, which limits the high current density in HER. Both kinetic analysis and theoretical calculations suggest that the Volmer step is the rate-limiting step. The high surface area of the NAC support boosts the HER current by maximizing exposed active species and minimizing mass transfer limitations. With a combination of high Co loading and large electrode surface area, enhanced kinetics enable Co-100-NAC-800 to overcome a large HER onset potential and access high current density (200 mA cm^{-2}) at moderate overpotential (310 mV) in LSV tests. In

addition, Co-NAC-800 demonstrates stability in HER over 100 h under strong alkaline conditions and at high current density, making it feasible for scalable industrial applications.

Methods

Materials

Iron(III) acetylacetonate (≥99.5%, trace metal), cobalt(II) acetylacetonate (≥99%), nickel(II) acetylacetonate (95%), copper(II) acetylacetonate (≥99.9%, trace metal), platinum(II) acetylacetonate (≥99.8%, trace metal), palladium(II) acetylacetonate (98%), carbon tetrachloride (≥99.9%), ethylenediamine (≥99.5%), tetraethyl orthosilicate (TEOS, 98%), and pluronic P123 (Mn~5800) were purchased from Sigma–Aldrich. Hydrofluoric acid (TraceMetal grade), hydrochloric acid (TraceMetal grade), and nitric acid (TraceMetal grade) were purchased from Fisher Chemical. All chemicals were used as received.

Synthesis of transition metal single-atom on NAC

Synthesis of SBA-15 template: SBA-15 with ordered pore structure was synthesized using P123 as the soft template.[35] In a 500 mL polypropene bottle, 4.0 g of P123 was added to HCl-H_2O solution (120 mL of 2 M HCl solution and 30 mL H_2O) and stirred at 36 °C oil bath for 1 h to dissolve P123. 8.5 g of TEOS was then added to the solution with stirring. The transparent solution slowly changed to milky white indicating the nucleation and growth of porous silica. After 20 h in 36 °C oil bath, the mixture was transferred to a 100 °C oven and stayed for another 24 h to age the formed silica. The mixture was then allowed to cool down to room temperature naturally. SBA-15 was separated by filtration and washed with water until pH neutral. After drying the solid at 75 °C overnight, the templating P123 was removed by calcination at 550 °C for 5h to enable the exposure of pore structures.

Synthesis of single-atom NAC: The desired amount of metal acetylacetonate was first dissolved into the solution of ethylenediamine (1.80 g). 4.0 g of carbon tetrachloride was then added, followed by adding 0.80 g of SBA-15. The mixture was heated in a 90 °C oil bath for 16 h for condensation. The oil bath temperature was then increased to 120 °C for 4 h to remove the uncondensed ethylenediamine and carbon tetrachloride. The obtained brown powders were calcined under Ar flow, with temperature raised at a ramping rate of 3 °C min^{-1} to 600, 700, or 800 °C and maintained for 2 h. After carbonization, the black powder was treated with 5 wt.% HF and 10 wt.% HCl aqueous solution for 2 days to remove SBA-15 template and excess metals. The products were recovered via centrifugation, washed with deionized water until the pH reached 7, and dried at 100 °C. The prepared single-atom NAC was named M-x-NAC-y, where M is the type of metal, x is the amount of metal acetylacetonate added in milligrams, and y is the calcination temperature in Celsius.

Synthesis of NAC: NAC was synthesized using the same method as the synthesis of single-atom NAC, but without adding metal acetylacetonate precursors.

Characterization

Powder X-ray diffraction (XRD) was performed using a Bruker D8A25 diffractometer with Cu *Kα* radiation (λ = 1.54184 Å). N_2 physisorption was performed using an auto-adsorption analyzer (Micromeritics, 3Flex) at −196 °C. Inductively coupled plasma mass spectroscopy (ICP-MS) for metal loadings was measured with a Thermo Scientific X Series 2 spectrometer. HAADF-STEM imaging was performed on a Titan Themis 300 equipped with a gun monochromator and probe spherical aberration (Cs) corrector operated at 200 kV. The EDS mapping data was collected with a Super-X EDX detector. CHNS analysis was conducted using an Elemetar UNICUBE Analyzer. X-ray adsorption spectroscopy (XAS) experiments, including X-ray absorption near edge structure (XANES) and extended X-ray absorption fine structure (EXAFS), were conducted at 7-BM QAS beamline in National Synchrotron Light Source II (NSLS-II) at Brookhaven National Laboratory. Co K-edge of Co-NAC samples were collected in fluorescence mode at room temperature and ambient pressure. Co foil was also collected to be a reference for energy calibration and drift correction of the monochromator.

Athena and Artemis from the Demeter software package were used to analyze data of each sample.[36, 37] FEFF program was used for the calculation and proper fitting of EXAFS spectra. And *k* range between 2.5 to 8.5 $Å^{-1}$ was used for Fourier-transformed (FT) EXAFS spectra.

Hydrogen evolution reaction

Working electrode preparation: 1 mg of prepared NAC or metal-NAC catalyst was dispersed in 0.49 mL of acetone and 10 µL of Nafion solution through sonication for 30 min. The suspension was dropcasted onto 1×2 cm^2 carbon fiber paper forming a 1×1 cm^2 catalyst patch. The electrode was dry at room temperature in a fume hood overnight.

H-cell HER test: HER was tested in a 3-electrode system using Biologic electrochemical potential station. Catalyst-loaded carbon fiber paper, Hg/HgO (1M KOH), and Pt mesh were used as the working, reference, and counter electrodes, respectively. The working and counter electrodes were separated with Nafion 212 membrane. The potential was converted from Hg/HgO to RHE using Equation 2. LSV was performed to evaluate the HER properties of NAC catalysts from 0 to -0.5 V vs RHE at a scan rate of 2 mV s^{-1} with 85% IR compensation.

$$E_{RHE} = E_{Hg/HgO} + E^{0}_{Hg/HgO} + 0.059pH \quad (2)$$

High current density HER tests: Large current HER was tested in a 3-electrode, 1-component cell using Biologic electrochemical potential station with a booster. NAC-loaded carbon fiber paper, Hg/HgO, and Pt plate were used as working, reference, and counter electrodes, respectively. The same LSV was

performed with 2mV s^{-1} scanning rate and 85 % IR compensation.

Stability test: A stability test was performed in the one-component cell. Chronopotentiometry (CP) under constant current (50 mA cm^{-2}) was applied, and the potential change was recorded for 20 h. During the stability test, a stir bar was added with 800 rpm stirring to minimize the external mass transfer limitation.

MEA test: The flow electrolyzer contains two stainless steel flow-field plates with serpentine channels, PTFE and silicone gaskets, and the MEA, which contains two electrodes and a membrane, was formed after assembling the cell hardware. Pt/C (0.5 $mg_{catalyst}$ cm^{-2}) and Co-NAC (1 $mg_{catalyst}cm^{-2}$) were spray-coated on HNO_3-treated carbon cloth substrates as the anode and cathode, respectively. The mass ratio of nanoparticles and ionomer was 4:1. The catholyte and anolyte of 1 M KOH were circulated by a peristaltic pump (Masterflex® L/S®) at 20 ml min^{-1}. The applied current was controlled by a Biologic SP-300 potentiostat/galvanostat. The membrane used to separate catholyte and anolyte was an anion exchange membrane (Tokuyama A201). The test was performed at room temperature.

Computational Details

The DFT calculations were performed using the VASP package.[38] The Perdew–Burke–Ernzerhof (PBE) functional within the generalized gradient approximation (GGA) was used for the exchange–correlation energy.[39] The electron–ion interaction was described by the projector augmented wave (PAW) approach.[40, 41] The van der Waals interaction was included using the DFT-D3 method.[42] All electronic energies were converged to 10^{-5} eV, and the atomic force on each atom was minimized to be less than 0.02 eV $Å^{-1}$. The structures of single atom NACs were taken from a previous work.[22] A (3 × 3 × 1) Monkhorst–Pack k-point was used to sample the first Brillouin zone. The Gibbs free energy of adsorption was computed using the computational hydrogen electrode model where the chemical potential of (H^++e^-) at pH=0 equaled the chemical potential of 1 bar H_2 in the gas phase at 298 K.[32, 34] We added 0.24 eV onto the DFT-calculated total energies to take into account the entropy lost and zero-point energy change for the adsorbed sate.[32]

Author Contributions

All authors contributed to the conceptualization. JY conducted the electrochemical evaluation and part of the materials characterization under the supervision of WH. YY performed the theoretical study under the supervision of BW. YL synthesized the materials and conducted part of the characterization under the supervision of ZZ, LQ, and WH. HL assisted with the electrochemical tests under the supervision of WL. SS assisted with the electrochemical tests under the supervision of WH. YL, SX, and FL conducted the XAS study. JY and YY drafted the manuscript under the supervision of BW and WH. YL and LQ drafted the XAS part of the manuscript. All authors contributed to the manuscript revision and finalization.

Conflicts of interest

There are no conflicts to declare.

Data availability

All data are available in the main text and the Supplementary Information.

Acknowledgments

This work is partially supported by NSF grant CHE-2108306/ 2108307 and the Trapp award from Iowa State University. L.Q. and Y.L. were supported by the U.S. Department of Energy (DOE), Office of Basic Energy Sciences, Division of Chemical Sciences, Geosciences, and Biosciences, Catalysis Science program. The Ames Laboratory is operated for the U.S. DOE by Iowa State University under Contract No. DE-AC02-07CH11358. Z.Z. was supported by NSFC grant 22078288. Y.L. was supported by International Doctoral Exchange Fellowship Program of Zhejiang University. The computations were performed at the OU Supercomputing Center for Education & Research and the National Energy Research Scientific Computing Center (NERSC), a U.S. Department of Energy Office of Science User Facility, and were supported by the U.S. Department of Energy, Basic Energy Sciences (Grant DE-SC0018284). This research used beamline 7-BM (QAS) of the National Synchrotron Light Source II, a U.S. Department of Energy (DOE) Office of Science User Facility operated for the DOE Office of Science by Brookhaven National Laboratory under Contract No. DE-SC0012704. All electron microscopy and related work were performed using instruments in the Sensitive Instrument Facility in Ames National Laboratory.

References

1. M. Zeng and Y. Li, *J. Mater. Chem. A*, 2015, **3**, 14942-14962.
2. Z. Zhao, H. Liu, W. Gao, W. Xue, Z. Liu, J. Huang, X. Pan and Y. Huang, *J. Am. Chem. Soc.*, 2018, **140**, 9046-9050.
3. F. Y. Yu, Z. L. Lang, L. Y. Yin, K. Feng, Y. J. Xia, H. Q. Tan, H. T. Zhu, J. Zhong, Z. H. Kang and Y. G. Li, *Nat Commun*, 2020, **11**, 490.
4. L. Zhang, H. Liu, S. Liu, M. Norouzi Banis, Z. Song, J. Li, L. Yang, M. Markiewicz, Y. Zhao, R. Li, M. Zheng, S. Ye, Z.-J. Zhao, G. A. Botton and X. Sun, *ACS Catal.*, 2019, **9**, 9350-9358.
5. T. He, W. Wang, F. Shi, X. Yang, X. Li, J. Wu, Y. Yin and M. Jin, *Nature*, 2021, **598**, 76-81.
6. Z. Shi, X. Zhang, X. Lin, G. Liu, C. Ling, S. Xi, B. Chen, Y. Ge, C. Tan, Z. Lai, Z. Huang, X. Ruan, L. Zhai, L. Li, Z. Li, X. Wang, G.-H. Nam, J. Liu, Q. He, Z. Guan, J. Wang, C.-S. Lee, A. R. J. Kucernak and H. Zhang, *Nature*, 2023, **621**, 300-305.
7. L. Liao, S. Wang, J. Xiao, X. Bian, Y. Zhang, M. D. Scanlon, X. Hu, Y. Tang, B. Liu and H. H. Girault, *Energy Environ. Sci.*, 2014, **7**, 387-392.

8. H. Wang, N. Ma, Y. Cao, H. Yu, J. Zuo, W. Fan and F. Peng, *International Journal of Hydrogen Energy*, 2019, **44**, 3649-3657.
9. H. Wang, X. Xiao, S. Liu, C. L. Chiang, X. Kuai, C. K. Peng, Y. C. Lin, X. Meng, J. Zhao, J. Choi, Y. G. Lin, J. M. Lee and L. Gao, *J. Am. Chem. Soc.*, 2019, **141**, 18578-18584.
10. X. Li, R. Zhang, Y. Luo, Q. Liu, S. Lu, G. Chen, S. Gao, S. Chen and X. Sun, *Sustainable Energy & Fuels*, 2020, **4**, 3884-3887.
11. T.-X. Huang, X. Cong, S.-S. Wu, J.-B. Wu, Y.-F. Bao, M.-F. Cao, L. Wu, M.-L. Lin, X. Wang, P.-H. Tan and B. Ren, *Nat. Catal.*, 2024, **7**, 646-654.
12. Q. Zhang and J. Guan, *Advanced Functional Materials*, 2020, DOI: 10.1002/adfm.202000768, 2000768.
13. Q. Yang, H. Liu, P. Yuan, Y. Jia, L. Zhuang, H. Zhang, X. Yan, G. Liu, Y. Zhao, J. Liu, S. Wei, L. Song, Q. Wu, B. Ge, L. Zhang, K. Wang, X. Wang, C.-R. Chang and X. Yao, *J. Am. Chem. Soc.*, 2022, **144**, 2171-2178.
14. R. Liu, Z. Gong, J. Liu, J. Dong, J. Liao, H. Liu, H. Huang, J. Liu, M. Yan, K. Huang, H. Gong, J. Zhu, C. Cui, G. Ye and H. Fei, *Adv. Mater.*, 2021, **33**, e2103533.
15. T. Sun, S. Zhao, W. Chen, D. Zhai, J. Dong, Y. Wang, S. Zhang, A. Han, L. Gu, R. Yu, X. Wen, H. Ren, L. Xu, C. Chen, Q. Peng, D. Wang and Y. Li, *Proc Natl Acad Sci U S A*, 2018, **115**, 12692-12697.
16. J. Li, H. Li, W. Xie, S. Li, Y. Song, K. Fan, J. Y. Lee and M. Shao, *Small Methods*, 2022, **6**, e2101324.
17. X. Liu, Y. Deng, L. Zheng, M. R. Kesama, C. Tang and Y. Zhu, *ACS Catal.*, 2022, DOI: 10.1021/acscatal.2c01253, 5517-5526.
18. X. Wan, X. Liu, Y. Li, R. Yu, L. Zheng, W. Yan, H. Wang, M. Xu and J. Shui, *Nat. Catal.*, 2019, **2**, 259-268.
19. D. Lyu, Y. Du, S. Huang, B. Y. Mollamahale, X. Zhang, S. W. Hasan, F. Yu, S. Wang, Z. Q. Tian and P. K. Shen, *ACS Appl. Mater. Interfaces*, 2019, **11**, 39809-39819.
20. Z. Yin, J. Yu, Z. Xie, S.-W. Yu, L. Zhang, T. Akauola, J. G. Chen, W. Huang, L. Qi and S. Zhang, *J. Am. Chem. Soc.*, 2022, **144**, 20931-20938.
21. Y. Lin, R. Nie, Y. Li, X. Wu, J. Yu, S. Xie, Y. Shen, S. Mao, Y. Chen, D. Lu, Z. Bao, Q. Yang, Q. Ren, Y. Yang, F. Liu, L. Qi, W. Huang and Z. Zhang, *Nano Research*, 2022, DOI: 10.1007/s12274-022-4294-6.
22. Z. Luo, Z. Yin, J. Yu, Y. Yan, B. Hu, R. Nie, A. F. Kolln, X. Wu, R. K. Behera, M. Chen, L. Zhou, F. Liu, B. Wang, W. Huang, S. Zhang and L. Qi, *Small*, 2022, **18**, 2107799.
23. T. Jiang and D. E. Ellis, *Journal of Materials Research*, 1996, **11**, 2242-2256.
24. G. Jacobs, Y. Ji, B. H. Davis, D. Cronauer, A. J. Kropf and C. L. Marshall, *Applied Catalysis A: General*, 2007, **333**, 177-191.
25. M. Hunault, G. Calas, L. Galoisy, G. Lelong and M. Newville, *J. Am. Ceram. Soc.*, 2014, **97**, 60-62.
26. C. Zhu, Q. Shi, B. Z. Xu, S. Fu, G. Wan, C. Yang, S. Yao, J. Song, H. Zhou, D. Du, S. P. Beckman, D. Su and Y. Lin, *Advanced Energy Materials*, 2018, **8**, 1801956.
27. Z.-L. Wang, X.-F. Hao, Z. Jiang, X.-P. Sun, D. Xu, J. Wang, H.-X. Zhong, F.-L. Meng and X.-B. Zhang, *J. Am. Chem. Soc.*, 2015, **137**, 15070-15073.
28. T. Shinagawa, A. T. Garcia-Esparza and K. Takanabe, *Scientific reports*, 2015, **5**, 13801.
29. Y. Xue, B. Huang, Y. Yi, Y. Guo, Z. Zuo, Y. Li, Z. Jia, H. Liu and Y. Li, *Nat Commun*, 2018, **9**, 1460.
30. C. C. L. McCrory, S. Jung, J. C. Peters and T. F. Jaramillo, *J. Am. Chem. Soc.*, 2013, **135**, 16977-16987.
31. D. Qu and H. Shi, *Journal of Power Sources*, 1998, **74**, 99-107.
32. J. K. Nørskov, T. Bligaard, A. Logadottir, J. R. Kitchin, J. G. Chen, S. Pandelov and U. Stimming, *J. Electrochem. Soc.*, 2005, **152**, J23.
33. V. Fung, G. Hu, Z. Wu and D.-e. Jiang, *The Journal of Physical Chemistry C*, 2020, **124**, 19571-19578.
34. J. K. Nørskov, J. Rossmeisl, A. Logadottir, L. Lindqvist, J. R. Kitchin, T. Bligaard and H. Jónsson, *The Journal of Physical Chemistry B*, 2004, **108**, 17886-17892.
35. D. Zhao, J. Feng, Q. Huo, N. Melosh, G. H. Fredrickson, B. F. Chmelka and G. D. Stucky, *Science*, 1998, **279**, 548-552.
36. D. Bazin and L. Guczi, *Appl. Catal. A-Gen.*, 2001, **213**, 147-162.
37. P. Serna and B. C. Gates, *Accounts Chem. Res.*, 2014, **47**, 2612-2620.
38. G. Kresse and J. Hafner, *Physical Review B*, 1993, **47**, 558-561.
39. J. P. Perdew, K. Burke and M. Ernzerhof, *Phys. Rev. Lett.*, 1996, **77**, 3865-3868.
40. P. E. Blöchl, *Physical Review B*, 1994, **50**, 17953-17979.
41. G. Kresse and D. Joubert, *Physical Review B*, 1999, **59**, 1758-1775.
42. S. Grimme, J. Antony, S. Ehrlich and H. Krieg, *The Journal of Chemical Physics*, 2010, **132**, 154104.

